Topographic Effects on the Surface Radiation Balance in and around Arizona's Meteor Crater

SEBASTIAN W. HOCH AND C. DAVID WHITEMAN

University of Utah, Salt Lake City, Utah

(Manuscript received 24 July 2009, in final form 8 December 2009)

ABSTRACT

The individual components of the slope-parallel surface radiation balance were measured in and around Arizona's Meteor Crater to investigate the effects of topography on the radiation balance. The crater basin has a diameter of 1.2 km and a depth of 170 m. The observations cover the crater floor, the crater rim, four sites on the inner sidewalls on an east–west transect, and two sites outside the crater. Interpretation of the role of topography on radiation differences among the sites on a representative clear day is facilitated by the unique symmetric crater topography. The shortwave radiation balance was affected by the topographic effects of terrain exposure, terrain shading, and terrain reflections, and by surface albedo variations. Terrain exposure caused a site on the steeper upper eastern sidewall of the crater to receive 6% more daily integrated shortwave energy than a site on the lower part of the same slope. Terrain shading had a larger effect on the lower slopes than on the upper slopes. At the lower western slope site the daily total was reduced by 6%. Measurements indicate a diffuse radiation enhancement due to sidewall reflections. The longwave radiation balance was affected by counterradiation from the crater sidewalls and by reduced emissions due to the formation of a nighttime temperature inversion. The total nighttime longwave energy loss at the crater floor was 72% of the loss observed at the crater rim.

1. Introduction

Net radiation is the most important component of the surface energy balance and the key determinant of the lower boundary condition for all processes that lead to a redistribution of energy within the atmospheric boundary layer. The effects of topography on the radiation balance lead to differing microclimates within mountainous terrain. The recent Meteor Crater Experiment (METCRAX; Whiteman et al. 2008) was conducted in and around Arizona's Meteor Crater (Fig. 1) during October 2006. During this experiment, extensive radiation data were collected in the unique, idealized topographic basin that was formed by a meteorite impact 40 km east of Flagstaff, Arizona, 49 000 yr ago (Phillips et al. 1991). This dataset provides a unique opportunity to evaluate topographic effects on surface radiative fluxes. This article summarizes the terrestrial (longwave) and solar (shortwave) radiation budgets from METCRAX.

Corresponding author address: Sebastian W. Hoch, University of Utah, 135 S 1460 E, Rm. 819, Salt Lake City, UT 84112-0110.
E-mail: sebastian.hoch@utah.edu

DOI: 10.1175/2010JAMC2353.1

2. Background

The shortwave radiation budget components can be quite variable in areas of complex topography because of the interplay between the seasonal and diurnal variations in the sun's position; variations in elevation, azimuth angle, and slope angle of inclined complex terrain surface elements (terrain exposure); the physical and vegetative properties of the surface elements; and the propagation of shadows from surrounding topography. Duguay (1993) summarized these interactions between the radiation field and topography, focusing on the challenge of modeling radiative fluxes in complex topography. While the effects of terrain exposure on the largest source term of the radiation balance during clear skies—the direct solar radiation—can be modeled quite well, uncertainties remain in the parameterization of diffuse sky radiation and of terrain-reflected shortwave radiation. The difficulty lies in dealing with anisotropic radiation fields. Chen et al. (2006) showed an increase in the importance of diffuse radiation at higher zenith angles, and the importance of terrain-reflected radiation during winter (higher surface albedo) and in deeper valleys.

Duguay (1993) also addressed the lack of knowledge on the interactions between topography and the longwave

FIG. 1. Aerial photograph of Meteor Crater from the southeast (©John S. Shelton, used with permission).

radiation field. Many of the available models use the assumption that the longwave radiance from surrounding terrain that replaces the radiation from the obstructed sky is isotropic. Because of these assumptions, and with the uncertainty of the role of infrared transmissivity, the effects of valley or basin sidewall counterradiation are still poorly known. Olyphant (1986) investigated the influence of longwave radiation from surrounding topography on the energy balance of alpine snowfields. He calculated that longwave loss is typically reduced by approximately 50% when compared to the ridgetops. Plüss and Ohmura (1997) addressed the influence of longwave counterradiation from elevated snow-covered terrain on the radiation balance in mountainous terrain. They stressed the importance of the influence of surface temperature of the sky-obstructing terrain but also of the air temperature between the point of interest and the surrounding terrain, an often neglected influence (Dirmhirn 1964). Plüss and Ohmura (1997) show that neglecting the effects of the usually warmer air temperatures leads to an underestimation of the radiation emitted from the obstructed parts of the hemisphere.

The influence of topography on the radiation budget—and therefore the surface energy budget—affects the quality of mesoscale weather forecasts. Müller and Scherer (2005) improved temperature forecasts with subgrid-scale parameterizations of topographic effects for areas dominated by wintertime shading, areas with increased daytime sun exposure, and deeper valleys where nighttime counterradiation is important. The impact of terrain shading on boundary layer evolution was studied by Colette et al. (2003), who found that shading significantly influences the timing of the modeled morning breakup of the nocturnal stable boundary layer in an idealized valley.

The variation of the radiation budget on the larger scale of typical mountain ranges like the Black Forest (Iziomon et al. 2001) and the Alps (Marty et al. 2002) has been addressed by previous studies. Regional and seasonal dependencies of radiation climates, and features such as cloud radiative forcing (Marty et al. 2002) or the greenhouse effect, (Philipona et al. 2004) have been investigated. These studies, however, are based on standard horizontal observations over representative surfaces.

Fewer studies have addressed the effects of smaller-scale topography on the radiation field arising from varying exposure, shading, and sky view effects as well as surface properties like albedo. These effects, the topic of this article, were previously investigated by Whiteman et al. (1989) and Matzinger et al. (2003) by measuring the radiative fluxes on surfaces parallel to the underlying topography. Whiteman et al. (1989) reported significant differences in the radiation budget for different physiographic regions in the northwest–southeast-oriented Brush Creek Valley for a clear-sky day. Incoming solar radiation increased with altitude. A higher daytime net radiation gain and a higher nighttime net radiation loss at a ridgetop site were attributed to its unobstructed view of the sky. Matzinger et al. (2003) report radiation measurements taken in a cross section through Switzerland's Riviera Valley. Key findings were a decrease in downward longwave radiation and an increase of net radiation with height. Oliphant et al. (2003) addressed the importance of different topographic or site-specific characteristics that influence the spatial variability in the radiation budget with a limited set of observations and additional model calculations. They found slope aspect and slope angle to be the most dominating characteristics, followed by elevation, albedo, shading, sky view factor, and leaf area index.

The motivation of the present study was to obtain a comprehensive complex terrain dataset accurately measuring all slope-parallel radiation budget components at representative sites in a simple terrain setting to quantify the importance of topographic influences on the radiation budget.

3. Observations, instrumentation, and instrument accuracies

Detailed observations of the shortwave and longwave components of the surface radiation budget were made at eight different sites during METCRAX. Radiation instruments were installed and operated by the National Center for Atmospheric Research.

The locations of the radiometer sites are shown in Fig. 2. The sites inside the crater were placed on an east–west line because of an experimental design that focused on boundary layer asymmetries during the morning and evening transition periods (Whiteman et al. 2008). Four of the sites—one on the crater floor, named Floor

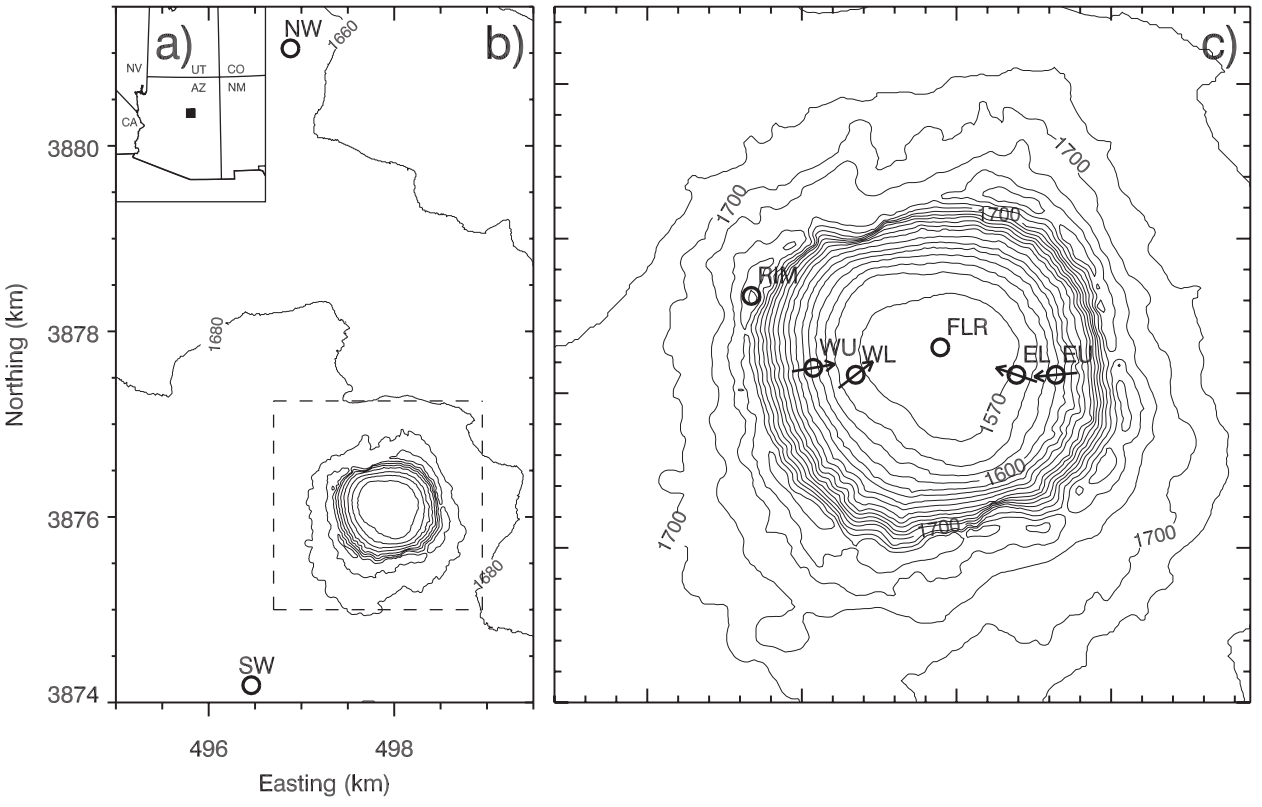

FIG. 2. (a) Universal transverse Mercator zone 12S map showing the location of Meteor Crater in Arizona, and (b) the NW and SW sites outside the crater topography at a contour interval of 20 m. (c) The area in the dashed square around Meteor Crater is expanded to show the locations of the remaining six sites at a contour interval of 10 m. Arrows at sidewall sites indicate the slope direction.

(FLR); one at the highest point on the west rim of the crater, named Rim (RIM); and two on the plain outside the crater, named Southwest (SW) and Northwest (NW)—were located over quasi-horizontal surfaces. The remaining four sites were located on the sloping inner sidewalls of the crater, two on the upper and lower west sidewall named West Upper (WU) and West Lower (WL) and two on the upper and lower east sidewall named East Upper (EU) and East Lower (EL). The semiarid sites all had widely distributed shrubs and grasses. Site photographs are shown in Fig. 3.

At the six sites within the crater basin, the four main components of the radiation balance (shortwave incoming or global $K\downarrow$, shortwave reflected $K\uparrow$, longwave incoming $L\downarrow$, and longwave outgoing $L\uparrow$ radiation) were measured individually, parallel to the slope of the underlying terrain, using Eppley Laboratory, Inc., Precision Spectral Pyranometers (PSP) or Kipp and Zonen, Inc., model CM21 pyranometers and Eppley Precision Infrared Radiometers (PIR) or Kipp and Zonen model CG4 pyrgeometers. Diffuse radiation $D\downarrow$ was measured at the crater rim and floor sites with Li-Cor, Inc., LI-200 silicon cell pyranometers and shadow bands. Direct shortwave radiation $S\downarrow$ was determined by subtracting $D\downarrow$ from $K\downarrow$ at the Rim and Floor sites. Table 1 summarizes the site locations and instrumentation and the exposure of the measurements (azimuth in degrees from north; slope angle).

A sawhorselike mounting system composed of a long rail with four adjustable-length A-frame legs was used to support the radiation instruments (Fig. 3). At the sloping sites, the rail was pointed up the crater sidewall along the line of the terrain gradient. The legs were adjusted so that the upper surface of the rail was parallel to the underlying sidewall slope. Slope surfaces are naturally quite inhomogeneous, so the slope surfaces to which the radiometers were oriented were averaged by eye over a scale of tens of meters. The exact instrument orientation was determined by a multilinear regression, fine-tuning measured azimuth and slope angles to fit the dataset. Data from the pyranometer at the Northwest site were corrected for a slight tilt ($<2°$).

Outside the crater at the Northwest and Southwest sites, net radiation Q^* was measured with Radiation and Energy Balance Systems, Inc., (REBS) Q7 net radiometers. In addition, $K\downarrow$ and $L\downarrow$ were monitored with the above-mentioned standard instrumentation at the Northwest site.

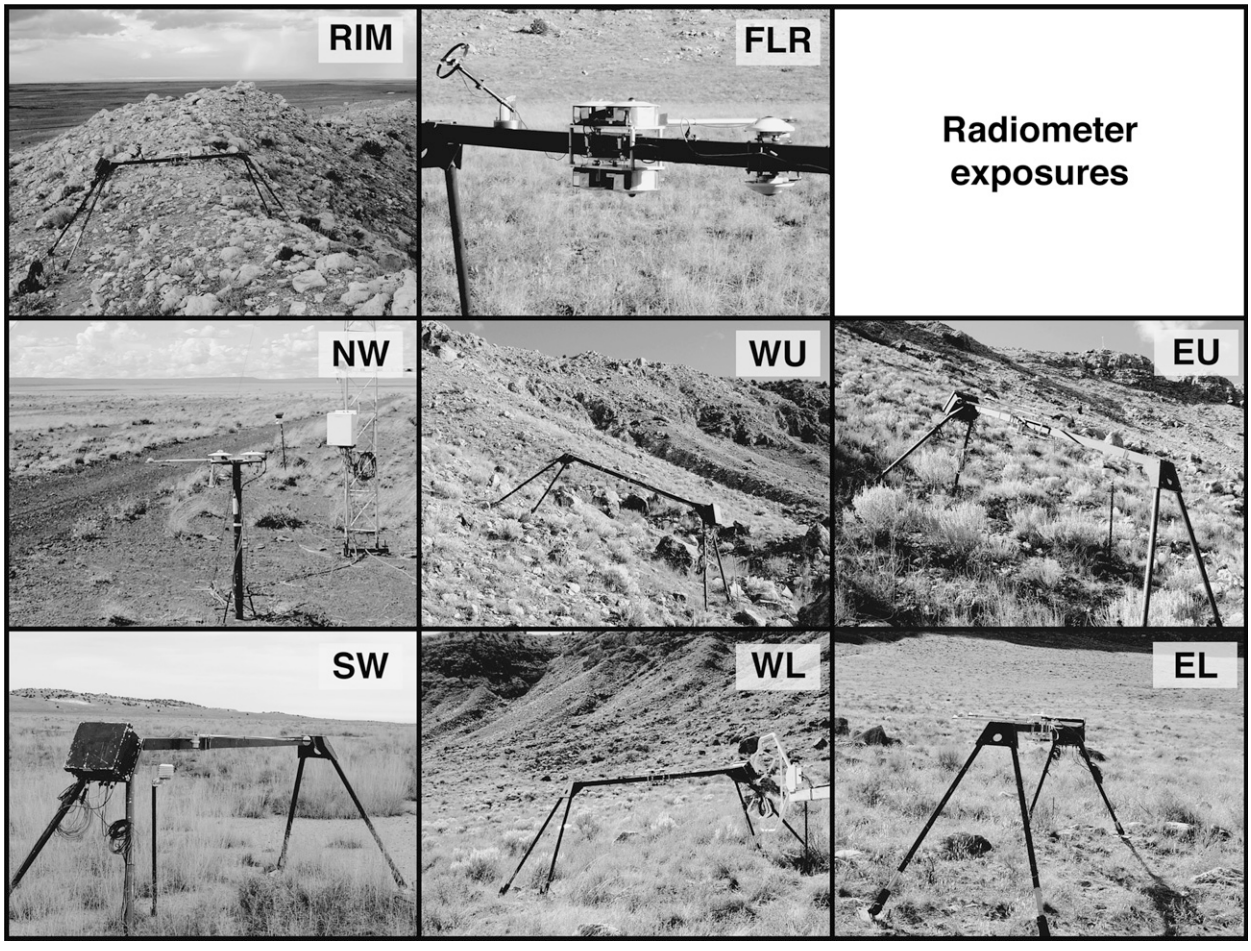

FIG. 3. Photographs of the radiation budget sites.

The leakage of shortwave radiation through the domes of Eppley PIR pyrgeometers is a known problem (Marty 2000). The pyrgeometers deployed during METCRAX had been characterized for their leakage during prior field deployments, and a correction depending on their exposure to global radiation was applied. This correction was largest for the pyrgeometer deployed at West Lower, amounting to 14 W m^{-2} at noon (19 W m^{-2} leakage per 1000 W m^{-2} global radiation).

The short METCRAX field study did not allow for extensive instrument intercomparisons. During METCRAX, however, the same instrumentation and mounting systems were used as during the Energy Balance Experiment (EBEX-2000; Oncley et al. 2007). We thus consider the

TABLE 1. Radiation measurement site characteristics.

Site identifier	Lon (°E)	Lat (°N)	Alt (m MSL)	Azimuth (°)	Slope (°)	Instruments*
RIM	−111.0292	35.0295	1744			PSP(u/d), PIR(u/d), Q7, LI-200
FLR	−111.0225	35.0280	1563			CM21(u/d), CG4(u/d), Q7, LI-200
WU	−111.0270	35.0274	1609	80.4	22.7	PSP(u/d), PIR(u/d), Q7
WL	−111.0255	35.0272	1572	52.3	5.3	PSP(u/d), PIR(u/d), Q7
EU	−111.0184	35.0272	1600	264.7	24.1	PSP(u/d), PIR(u/d), Q7
EL	−111.0198	35.0272	1572	288.8	5.7	PSP(u/d), PIR(u/d), Q7
SW	−111.0388	35.0103	1697			Q7
NW	−111.0342	35.0722	1670			PSP(u), PIR(u), Q7

* Q7 = REBS Q7 net radiometer; u/d = upward- and downward-looking pair; u = upward looking; and d = downward looking.

accuracies determined carefully during EBEX-2000 to be representative for our measurements. Kohsiek et al. (2007) report the following accuracies—incoming shortwave: maximum of 5 W m^{-2} or 1% of value; incoming longwave: 10 W m^{-2} (daytime), 5 W m^{-2} (nighttime); outgoing shortwave: maximum of 5 W m^{-2} or 6% of value; outgoing longwave: 10 W m^{-2} (daytime), 5 W m^{-2} (nighttime); and net radiation from four components: maximum of 25 W m^{-2} or 5% of value (daytime), 10 W m^{-2} (nighttime). Net radiation from REBS Q7 showed daytime underestimations by 20–40 W m^{-2} and nighttime overestimations by 10–20 W m^{-2} (Kohsiek et al. 2007).

Accuracy determinations for the LI-200 pyranometers used for diffuse radiation measurements are not available from EBEX-2000. The LI-200 pyranometer in its shadowband at Floor was calibrated against the pyranometer measuring global radiation during field periods when both of these radiometers were in shadow (i.e., between astronomical and local sunrises and sunsets). Unfortunately, the diffuser of the LI-200 pyranometer at the Rim site was scratched during installation and replaced before the postexperimental recalibration. We thus have only the field data to infer a valid coefficient for the scratched sensor. This was done by comparing the relationships between the global and diffuse radiation measurements at the two sites, Floor and Rim, and by choosing a suitable coefficient for the LI-200 at Rim to reach a similar relationship to that seen at Floor. Nevertheless, we concluded after much analysis that the remaining uncertainty is too large to draw conclusions about the differences in diffuse radiation between the Rim and Floor site.

Data reported here are 5-min means of radiation data sampled at 5-s intervals, with the resulting average labeled with the ending time of the 5-min period. All times are mountain standard time (MST). The sign convention is that radiative fluxes directed toward the surface are positive and those directed away from the surface are negative, so that net radiation is given by

$$Q^* = K^* + L^* = \mathrm{K}\downarrow + \mathrm{K}\uparrow + \mathrm{L}\downarrow + \mathrm{L}\uparrow, \qquad (1)$$

where K^* is net shortwave radiation and L^* is net longwave radiation.

4. Results for 21 October 2006

A series of four clear days occurred during the period 19–22 October 2006. There was little variation in radiative components from day to day at individual sites during this period, so that the day with no missing data at any of the sites, 21 October, is chosen to illustrate the diurnal variation of the radiative fluxes. Figure 4 shows the observed radiative fluxes for the individual eight sites while Fig. 5 shows an intersite comparison of selected radiative quantities. Table 2 lists the daily radiation totals and the totals for both the astronomical and local day- and nighttime periods confined by the times of the astronomical sunrise (ASR), astronomical sunset (AST), local sunrise (LSR), and local sunset (LST). Times of the local sunrise and sunset were calculated with Corripio's (2003) shading algorithm. Table 3 provides ratios for selected radiation totals from Table 2, while Table 4 lists integrated values of the components of the shortwave radiation balance.

a. Extraterrestrial solar radiation

Extraterrestrial solar radiation $\mathrm{K}\downarrow_{\mathrm{ext}}$ is the theoretical radiation that would reach an unobstructed, homogeneous surface parallel to the terrain, under the assumption of no atmospheric attenuation; $\mathrm{K}\downarrow_{\mathrm{ext}}$ was computed for all sites and is shown in Fig. 4. The daily total extraterrestrial radiation was 24.37 MJ m^{-2} at the horizontal sites but varied from 22.38 to 25.14 MJ m^{-2} at the sloping sites (Table 2). Astronomical sunrise, solar noon, and astronomical sunset were at 0639, 1209, and 1738 MST, respectively. The minimum solar zenith angle attained at solar noon was 45.88°. The calculated curves of $\mathrm{K}\downarrow_{\mathrm{ext}}$ at the sloping sites (West Upper, West Lower, East Upper, and East Lower) shown in Fig. 4 indicate that the local sunrises would have occurred at 0639, 0639, 0823, and 0712 MST and local sunsets would have occurred at 1555, 1719, 1739, and 1739 MST, respectively. In actuality, terrain shading from the crater rim causes the local sunrise to be delayed and local sunset to be advanced at sites inside the crater, a phenomenon to be quantified in section 4e.

b. Incoming solar radiation

Global radiation $\mathrm{K}\downarrow$ is the sum of the direct solar radiation $\mathrm{S}\downarrow$ and the diffuse radiation $\mathrm{D}\downarrow$, the two subcomponents that will be discussed in more detail in the next subsection. At the horizontal sites, $\mathrm{K}\downarrow$ is symmetric about solar noon (Figs. 4, 5). At the sloping sites, however, the time of maximum receipt of $\mathrm{K}\downarrow$ depends strongly on the orientation of the slope and its exposure to the direct solar beam. Thus, the west sidewall insolation maxima are reached before noon and the east sidewall maxima are observed after noon. Generally, $\mathrm{K}\downarrow$ is smaller than extraterrestrial radiation because of atmospheric attenuation. The high altitude (approximately 1700 m) of Meteor Crater and its relatively aerosol-free air (compared to lower-elevation urban areas) minimize the attenuation of the solar beam. The daily total $\mathrm{K}\downarrow$ amounts to between 71% and 77% of $\mathrm{K}\downarrow_{\mathrm{ext}}$ at the individual sites (Table 3).

At the sites not affected by terrain shading, local sunrise and sunset are identical with astronomical sunrise and sunset. Within the crater basin, however, shadows cast by the surrounding higher topography of the crater sidewalls cause local sunrise to be delayed and local sunset to be

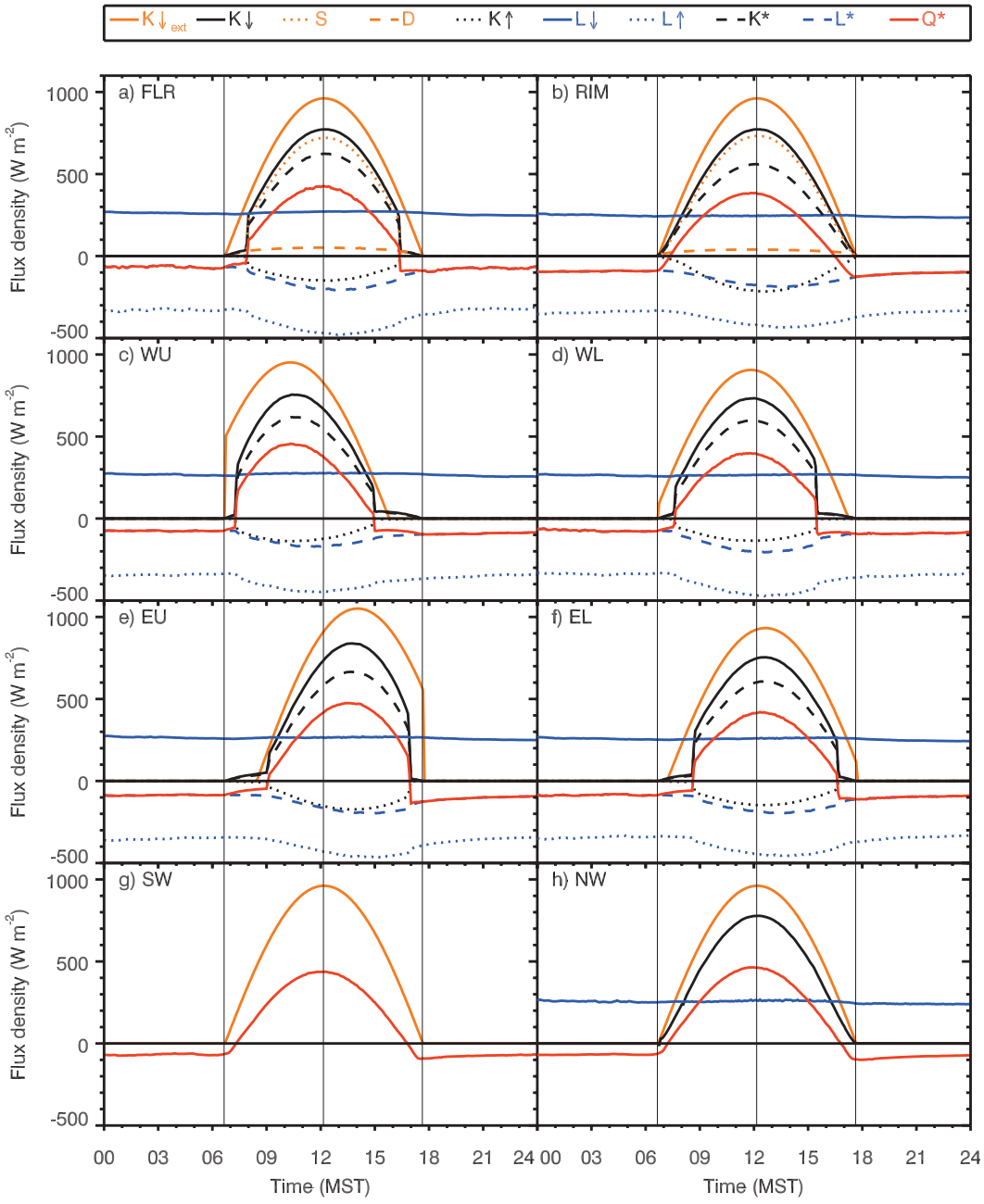

FIG. 4. Measured radiative fluxes (W m^{-2}) at the eight METCRAX sites on 21 Oct 2006. The thin vertical lines denote ASR, solar noon, and AST. Variable names are defined in the text.

advanced relative to the astronomical sunrise and sunset times. The sites from west to east in the crater (West Upper, West Lower, Floor, East Lower, and East Upper) experience delays in the local sunrise of 35, 55, 70, 115, and 140 min and advances in the local sunset of 160, 130, 75, 55, and 40 min, respectively (Table 2). While the obstructed sites still receive some diffuse radiation (section 4c), the period of direct insolation is reduced from 660 min at the unobstructed sites to 465, 475, 515, 490, and 480 min at the West Upper, West Lower, Floor, East Lower, and East Upper sites. The reduced daylight period caused by terrain shading (further quantified in section 4e) and the effects of terrain exposure (i.e., slope and azimuth angles) affect the daily totals. The unobstructed Rim and Northwest sites receive 18.84 and 18.69 MJ m^{-2} of radiation, respectively, between local sunrise and local sunset, while the obstructed, but horizontal, Floor site receives only 17.85 MJ m^{-2}. The West Upper and West

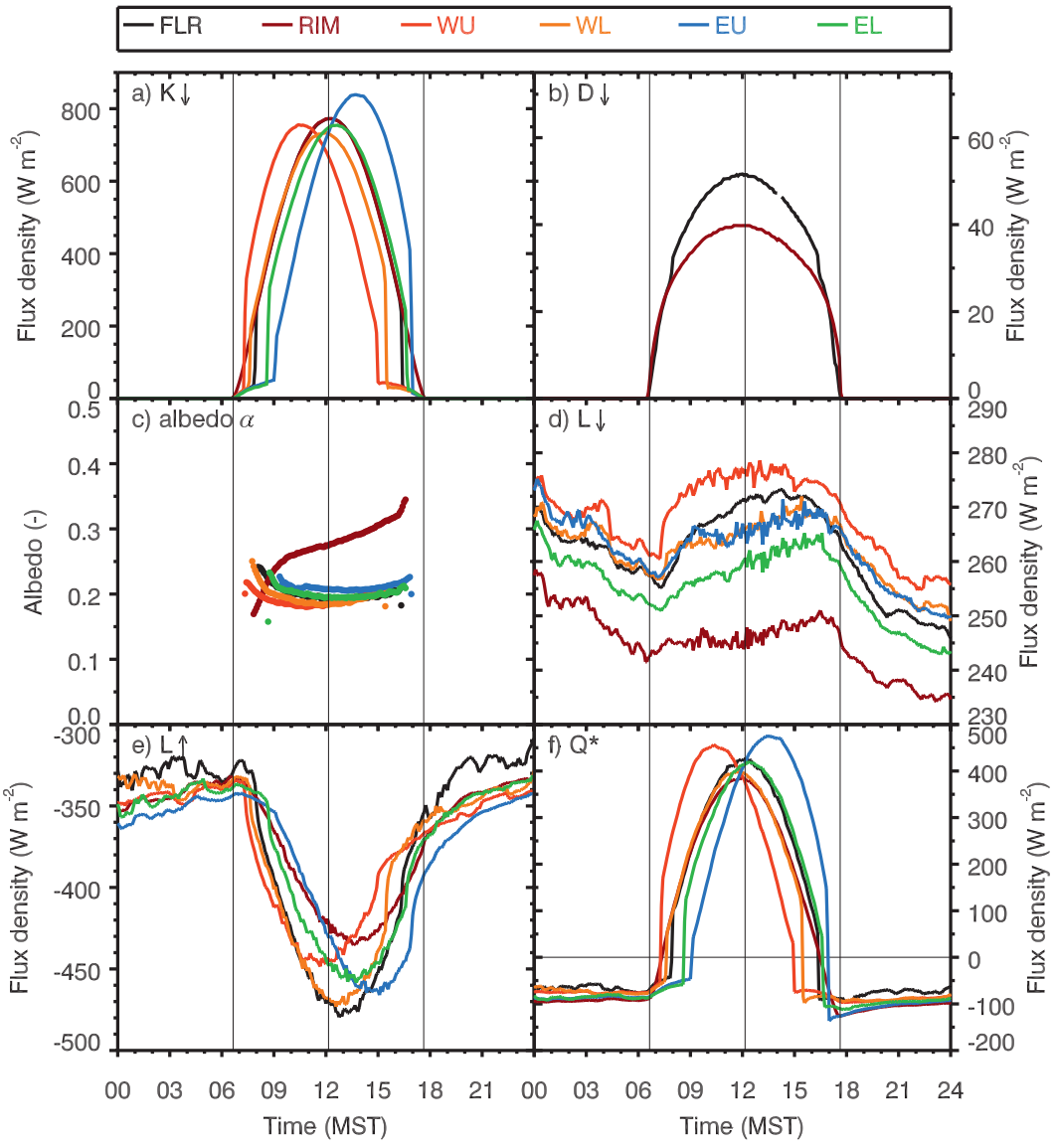

FIG. 5. Diurnal variation of selected radiative quantities (W m^{-2}) at the eight sites on 21 Oct 2006. (a) Global radiation on slope, (b) diffuse radiation, (c) albedo, (d) incoming longwave, (e) outgoing longwave, and (f) net radiation.

Lower sites receive similar incoming radiation totals—15.83 and 15.98 MJ m^{-2}, respectively, while the East Upper site is more favored in its receipt of K↓ relative to the East Lower site, 17.75 versus 16.71 MJ m^{-2} (Table 2). All instruments except the East Upper pyranometer are oriented slightly toward the north (Table 1). The steep slope angle at East Upper combined with the slight southerly exposure causes the high afternoon maximum in K↓ (Fig. 5a) and the largest of the daily K↓ totals observed at the sloping sites—a result of the smallest angles between the surface normal and the direct solar beam. In contrast, the potentially receipt-enhancing effect of a large slope angle at West Upper is reduced by the site's exposure toward north. The comparison of the two lower sidewall sites with similar slope angles shows the effect of the slope azimuth—the more northward-oriented West Lower site receives 4.6% less K↓ than East Lower, although some of this difference can be attributed to a larger impact of terrain shading (section 4e).

c. *Direct and diffuse solar radiation at the rim and floor of Meteor Crater*

During clear days, global radiation K↓ is dominated by direct solar radiation component S↓, while the diffuse solar radiation component D↓ plays only a secondary role; D↓ is the sum of the diffuse sky radiation

TABLE 2. Radiation totals (MJ m^{-2}) calculated from 5-min averages for 21 Oct 2006, where *N* indicates the number of 5-min intervals in the totals.

Site	Time (MST)	$K\downarrow_{ext}$	K↓	K↑	*K**	L↓	L↑	*L**	*Q**	*N*
Daily										
FLR	0000–2400	24.37	18.01	−3.56	14.45	22.64	−32.02	−9.37	5.07	288
RIM	0000–2400	24.37	18.85	−5.19	13.65	21.18	−31.76	−10.58	3.07	288
WU	0000–2400	22.38	16.14	−3.02	13.11	23.20	−32.32	−9.12	4.00	288
WL	0000–2400	22.68	16.20	−3.10	13.10	22.67	−32.44	−9.77	3.33	288
EU	0000–2400	25.14	18.02	−3.76	14.26	22.68	−32.84	−10.16	4.10	288
EL	0000–2400	23.43	16.92	−3.36	13.56	22.10	−32.33	−10.23	3.33	288
SW	0000–2400	24.37								288
NW	0000–2400	24.37	18.69			21.84				288
ASR–AST										
FLR	0640–1740	24.37	18.01	−3.56	14.45	10.59	−16.63	−6.03	8.41	132
RIM	0640–1740	24.37	18.84	−5.19	13.65	9.76	−15.69	−5.93	7.72	132
WU	0640–1740	22.38	16.13	−3.02	13.11	10.84	−16.07	−5.23	7.88	132
WL	0640–1740	22.68	16.20	−3.10	13.10	10.51	−16.45	−5.95	7.16	132
EU	0640–1740	25.14	18.02	−3.76	14.26	10.50	−16.21	−5.71	8.54	132
EL	0640–1740	23.43	16.92	−3.36	13.56	10.25	−16.19	−5.94	7.62	132
SW	0640–1740	24.37								132
NW	0640–1740	24.37	18.69			10.20				132
AST–ASR										
FLR	1740–0640	0.00	0.00	0.00	0.00	12.05	−15.39	−3.34	−3.34	156
RIM	1740–0640	0.00	0.00	0.00	0.00	11.42	−16.07	−4.65	−4.65	156
WU	1740–0640	0.00	0.00	0.00	0.00	12.36	−16.24	−3.88	−3.88	156
WL	1740–0640	0.00	0.00	0.00	0.00	12.16	−15.99	−3.83	−3.83	156
EU	1740–0640	0.00	0.00	0.00	0.00	12.18	−16.63	−4.44	−4.44	156
EL	1740–0640	0.00	0.00	0.00	0.00	11.85	−16.14	−4.29	−4.29	156
SW	1740–0640	0.00								156
NW	1740–0640	0.00	0.00			11.65				156
LSR–LST										
FLR	0750–1625	22.93	17.85	−3.55	14.30	8.32	−13.59	−5.27	9.03	103
RIM	0640–1740	24.37	18.84	−5.19	13.65	9.76	−15.69	−5.93	7.72	132
WU	0715–1500	20.92	15.83	−2.99	12.84	7.66	−11.75	−4.08	8.76	93
WL	0735–1530	20.61	15.98	−3.07	12.90	7.57	−12.44	−4.87	8.03	95
EU	0900–1700	23.44	17.75	−3.72	14.03	7.67	−12.34	−4.67	9.36	96
EL	0835–1645	21.65	16.71	−3.33	13.38	7.65	−12.59	−4.94	8.44	98
SW	0640–1740	24.37								132
NW	0640–1740	24.37	18.69			10.20				132
LST–LSR										
FLR	1625–0750	1.44	0.16	−0.01	0.15	14.33	−18.43	−4.11	−3.95	185
RIM	1740–0640	0.00	0.00	0.00	0.00	11.42	−16.07	−4.65	−4.65	156
WU	1500–0715	1.47	0.30	−0.03	0.27	15.54	−20.57	−5.03	−4.76	195
WL	1530–0735	2.07	0.22	−0.03	0.20	15.10	−20.00	−4.90	−4.70	193
EU	1700–0900	1.70	0.28	−0.04	0.23	15.01	−20.50	−5.49	−5.26	192
EL	1645–0835	1.78	0.21	−0.03	0.18	14.45	−19.74	−5.29	−5.11	190
SW	1740–0640	0.00								156
NW	1740–0640	0.00	0.00			11.65				156

and downwelling shortwave terrain-reflected radiation. On 21 October D↓ accounted for only 9% of the K↓ at the crater floor (Table 3).

The diurnal variations of diffuse radiation for 21 October are shown in Fig. 5b. The large uncertainty in the diffuse observations at Rim due to its scratched diffuser needs to be kept in mind (section 3). Nevertheless we try to infer some information from the comparison of diffuse radiation at the two sites. At Rim, diffuse radiation was fairly symmetrical about solar noon, when it reached its maximum of approximately 40 W m^{-2}. Before local sunrise and after local sunset, the diffuse radiation at Floor closely matched the diffuse radiation at Rim. As soon as the Floor site was in direct sunlight, however, diffuse radiation at Floor exceeded that at Rim. The exceedance at Floor began near local sunrise when it rose suddenly by approximately 5 W m^{-2}. The excess at Floor reached 12 W m^{-2} by solar noon. After solar noon the excess decayed and then fell suddenly by approximately 5 W m^{-2} at local sunset, making the afternoon curve

TABLE 3. Ratios of selected radiation totals from Table 2.

Site	$K\downarrow_{ext}/K\downarrow_{ext}$ (RIM)	$K\downarrow/K\downarrow_{ext}$	$\lvert K\uparrow/K\downarrow\rvert$	$Q^*/K\downarrow_{ext}$	$Q^*/K\downarrow$	$D\downarrow/K\downarrow$
Daily						
FLR	1.00	0.74	0.20	0.21	0.35	0.09
RIM	1.00	0.77	0.28	0.13	0.22	0.07
WU	0.92	0.72	0.19	0.18	0.30	
WL	0.93	0.71	0.19	0.15	0.25	
EU	1.03	0.72	0.21	0.16	0.29	
EL	0.96	0.72	0.20	0.14	0.25	
SW	1.00			0.24		
NW	1.00	0.77		0.26		
LSR–LST						
FLR	0.94	0.78	0.20	0.39	0.63	0.08
RIM	1.00	0.77	0.28	0.32	0.57	0.07
WU	0.86	0.76	0.19	0.42	0.68	
WL	0.85	0.78	0.19	0.39	0.62	
EU	0.96	0.76	0.21	0.40	0.67	
EL	0.89	0.77	0.20	0.39	0.63	
SW	1.00			0.38		
NW	1.00	0.77		0.41		

a mirror image of the morning curve. The enhanced diffuse radiation at the crater floor relative to the crater rim appears to be caused by reflections from the surrounding topography. The amount of diffuse radiation received before local sunrise and after local sunset can be determined for the in-crater sites by subtracting the local sunrise to local sunset (LSR–LST) incoming radiation total from the astronomical sunrise to sunset (ASR–AST) total listed in Table 2. These diffuse radiation totals are 0.30, 0.22, 0.16, 0.20, and 0.27 MJ m^{-2} for West Upper, West Lower, Floor, East Lower, and East Upper, respectively, representing less than 2% of the daily total incoming solar radiation. Note, however, that the diffuse radiation received at Floor between local and astronomical sunrise and sunset, although small, constitutes 10% of the daily total diffuse radiation (1.54 MJ m^{-2}; Table 4).

d. Reflected shortwave radiation and albedo

Albedo α, the absolute value of the ratio of reflected to incoming radiation, varies throughout the day (Fig. 5c). Usually, over uniform and homogeneous surfaces, higher albedo values are observed after local sunrise, with lower values in midday, and higher values again prior to sunset, due to a higher reflectivity of natural surfaces at high zenith angles. Sites in Meteor Crater generally followed this pattern, with mean values of albedo between local sunrise and sunset generally between 0.19 and 0.21 (Table 3). The Rim site was the exception. A higher mean albedo of 0.28 was observed there, consistent with the lack of vegetation and exposure of bare rock and higher albedo ejecta from the crater. The site also exhibits an unusual diurnal variation of albedo: albedo increased monotonically during the day from 0.16 at local sunrise to 0.35 at local sunset. This site, located in a shallow saddle on the northwest rim, is approximately 20 m north of and a few meters below a high point on the crater rim. The surface directly below the downward-facing pyranometer was near horizontal, but the larger surroundings rapidly dropped off toward the southeast (into the crater) and more gently toward the west (toward the surrounding plain) but were raised toward the south (Barringer Point) and northeast (another high point on the crater rim). We speculate that the diurnally varying contributions of anisotropically reflected direct solar radiation on these differently exposed nearby surface elements to the upwelling shortwave flux are the dominating factor for this special diurnal albedo cycle.

TABLE 4. Integrated totals (MJ m^{-2}) of extraterrestrial, direct, diffuse, and incoming shortwave radiation for FLR and RIM for 21 Oct 2006.

Period	Time (MST)	$K\downarrow_{ext}$	$S\downarrow$	$D\downarrow$	$K\downarrow$
FLR					
Daily	0000–2400	24.37	16.47	1.54	18.01
ASR–AST	0640–1740	24.37	16.47	1.53	18.01
AST–ASR	1740–0640	0.00	0.00	0.00	0.00
LSR–LST	0750–1625	22.93	16.46	1.39	17.85
LST–LSR	1625–0750	1.44	0.01*	0.15	0.16
RIM					
Daily	0000–2400	24.37	17.59	1.26	18.85
ASR–AST	0640–1740	24.37	17.59	1.26	18.84
AST–ASR	1740–0640	0.00	0.00	0.00	0.00

* This value is an artifact arising from small differences between $K\downarrow$ and $D\downarrow$ within the observational uncertainty.

e. Quantifying the effects of terrain shading

In this section we wish to make the distinction between *terrain shading* and *self-shading*. Terrain shading occurs when higher terrain casts a shadow onto a surface. Self-shading occurs when a sloping surface not surrounded by obstructions faces away from, and is thus not illuminated by, the sun.

The effect of terrain shading can be calculated by subtracting observed global radiation $K\downarrow$ from potential global radiation $K\downarrow_p$, which is the shortwave radiative flux that would be received by a surface if it was not shaded by surrounding terrain. For times when no shading occurs, $K\downarrow_p$ is the same as $K\downarrow$. When shading occurs, $K\downarrow_p$ can be parameterized as

$$K\downarrow_p = K\downarrow_{ext} T_g^m, \tag{2}$$

where T_g is the global transmissivity and m is the optical air mass. We determine T_g from $K\downarrow$ and $K\downarrow_{ext}$ using data collected just before local sunset and just after local sunrise.

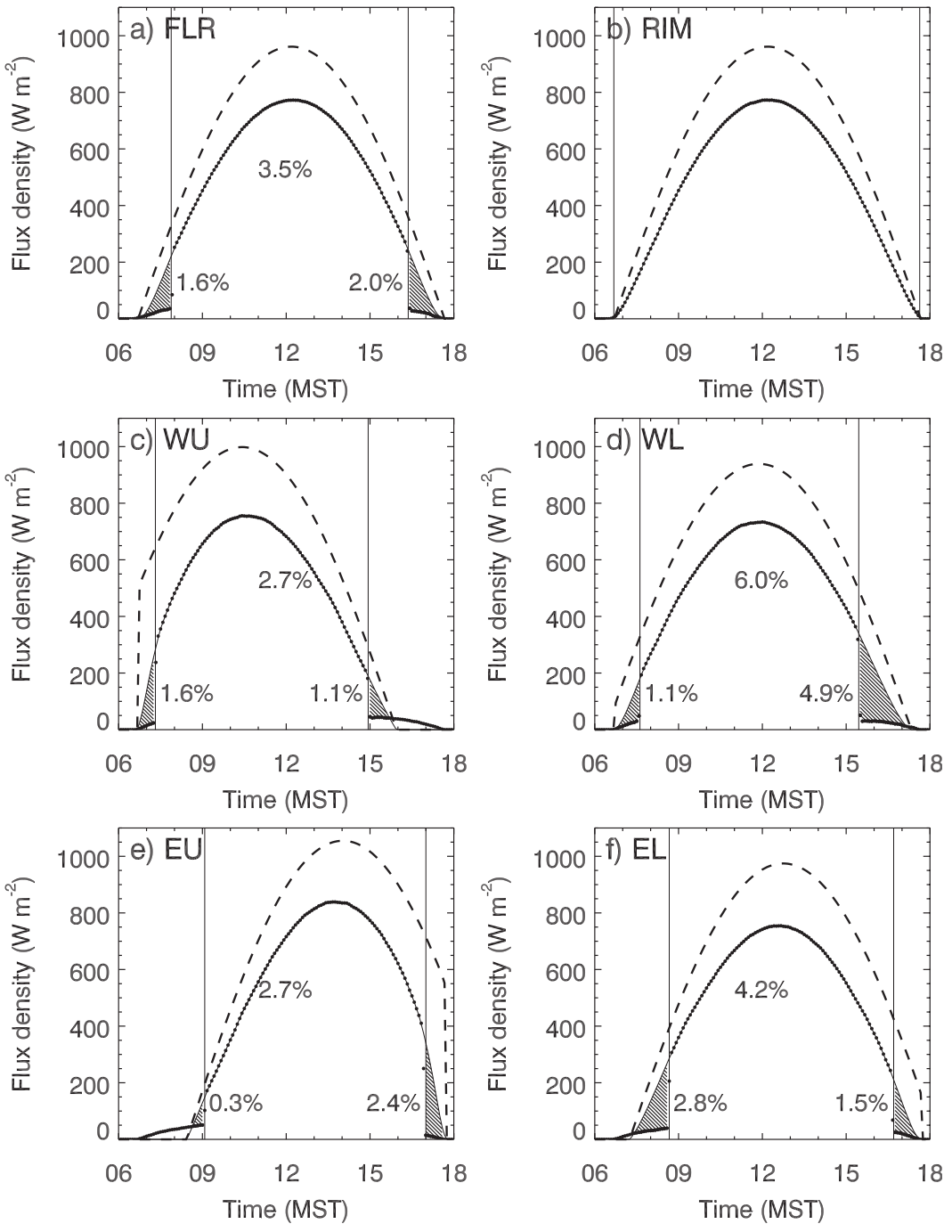

FIG. 6. Shadow effects on the receipt of global radiation (W m^{-2}). Shown are estimates of the percentage of global radiation that is lost during presunrise, daily, and postsunset periods because of terrain shading. The dashed curves are extraterrestrial radiation on the sloping surface, thin solid lines are the potential global radiation, and dotted curves are the observed global radiation. The hatched areas indicate the missing amounts of radiation caused by shadows. Note that diffuse radiation is received even when the sites are in shadow.

Terrain shading effects vary within Meteor Crater (Fig. 6). The highest reduction in insolation by terrain shading is observed at West Lower, where 6.0% is lost, while the lowest losses (2.7%) are seen at West Upper and East Upper. At Floor, the total loss amounts to 3.5%.

The reduction in shortwave radiation receipt in the evening due to terrain shading amounts to 1.1% at West

Upper but 4.9% at West Lower. This result is counterintuitive at first glance, as shadows occur 30 min sooner at West Upper than at West Lower. The potential global radiation, however, is already much smaller at West Upper than at West Lower when it is reached by the shadows cast from the rim. Also, the time span between the entry into shadow and the time when self-shading would occur is shorter at the upper site than at the lower site because of the different slope angles. The corresponding effect is seen at the east sidewall in the morning, where terrain shading reduces K↓ by only 0.3% of the potential global radiation at East Upper but by 2.8% at East Lower.

f. Incoming longwave flux

Figures 4 and 5d show incoming longwave radiation L↓. On 21 October, the observations of L↓ are all within a 20 W m^{-2} range during the night and a 30 W m^{-2} range during the day. The differences in L↓ between sites are thus only approximately twice as large as the observational uncertainty (section 3).

Over unobstructed horizontal surfaces, L↓ originates as thermal emissions from the overlying atmosphere and clouds. When higher topography surrounds an observation site, however, radiation emitted from the surrounding slopes increases the receipt of L↓, since the slopes radiate as gray bodies and are usually at a higher temperature than the effective radiating temperature of the sky. Warmer air above a site also increases L↓. Reflected longwave radiation is usually so small that it is not considered, as the emissivity of natural surfaces is normally above 0.95.

During both night and day, L↓ is lowest at Rim. This pattern is expected at night from the lack of surrounding topography and during daytime from the cooler air temperatures of the adjacent air (temperatures generally decrease with elevation from the crater floor when the atmosphere is well mixed during daytime). At the slope sites, in contrast, the warmer air and surrounding terrain lead to higher values of L↓ during daytime.

Generally L↓ increases at all sites as the atmosphere and surface warm during daytime and decreases as the atmosphere and surface cool during nighttime. There is an asymmetry between the morning increase in L↓ and the nighttime decrease, with the increase being particularly sharp at the west sidewall sites (Fig. 5d). The rapidly steepening terrain just above West Upper may subject this site to increasing downward irradiance from the nearby heated terrain just uphill from this site. The strong solar insolation just after sunrise (Fig. 5a) also leads to the rapid development of a convective or even superadiabatic air layer, which will contribute to the rapid increase in L↓. A sudden drop-off is not seen after local sunset, as the terrain retains much of the heat and only slowly cools on the surface, and colder air forming over the cooling slope stays shallow as it drains downslope.

In general, there was an asymmetry between the rapid rate of increase in L↓ in the morning and the slower rate of decrease in the afternoon. The rapid increase may be caused by the fast buildup of a near-surface warm air layer after sunrise. The slower decrease may be the result of the effective removal of cold air by drainage flows on the slopes.

g. Outgoing longwave flux

The outgoing longwave flux L↑ is the product of the fourth power of the effective radiating temperature, the emissivity of the underlying surface, and the Stefan–Boltzmann constant (Stefan–Boltzmann law). In the case of our slope-parallel measurements, the radiometer is exposed mostly to the nearby underlying ground. Most natural surfaces have an emissivity near or above 0.95 so that L↑ shown in Fig. 5e can be interpreted as a remote measurement of the effective radiating temperature of the underlying ground. On clear, undisturbed nights, a strong temperature inversion typically forms in the lowest 30 m above the crater floor, with an approximately isothermal layer above that extending to the crater rim (Whiteman et al. 2008). Because the lowest temperatures occur on the crater floor, |L↑| at Floor is weaker than at the other sites. Nocturnal temperature oscillations on the crater floor, typical of basins, are also clearly visible in Fig. 5e. As the sunlight moves down the west sidewall in the morning and the shadow from the crater rim retreats eastward and southward across the crater, |L↑| rises first at West Upper, then at West Lower, Floor, East Lower, and East Upper. The Rim site is a special case as it is ventilated by winds above the crater, remaining cooler than most of the interior sites in the morning and not cooling as fast as the other sites in the evening. The matching timing of this morning increase in |L↑| with the timing of the local sunrise indicates the fast response of L↑ to changes in shortwave insolation.

h. Net radiation

Slope-parallel net radiation Q^* was calculated as the sum of the four measured shortwave and longwave incoming and outgoing components with the exception of the two sites NW and SW where only observations from net radiometers were available. The main driving term in the surface energy balance is Q^*, and spatial differences in Q^* across the crater will influence the magnitudes of sensible, latent, and ground heat fluxes and thus their influences on the evolution of the atmospheric boundary layer. Shortly after sunset, Q^* reaches its minimum when the radiating temperature differences between the atmosphere and the surface are greatest. The time of maximum

Q^* at a level surface is usually shortly before solar noon, which is because the net longwave loss is larger after noon (Fig. 5f), while the net shortwave gain peaks exactly at solar noon (Fig. 5a). At the slope sites, the time of maximum Q^* is shifted analogously to the incoming shortwave radiation, with a maximum before noon on the west sidewall and after noon on the east sidewall.

Over the 24-h day, Q^* varied between 3.07 MJ m^{-2} at the Rim site and 5.07 MJ m^{-2} at the Floor site. Thus, 40% less net radiative energy was received at Rim than on the crater floor. This difference has shortwave and longwave contributions, explaining 40% and 60% of this difference, respectively. Despite the reduction of K↓ due to terrain shading at Floor, the lower albedo led to a higher K^*. On the longwave side, an increased L↓ reduced the net longwave loss. While the shortwave influence occurs during the day, the longwave influence acts throughout the 24-h period. During the day, the influence of the increase in L↓ is compensated for by the increased |L↑|. During the night, however, both a decreased |L↑| and an increased L↓ contribute to the longwave enhancement.

At the upper sidewall sites, East Upper and West Upper, the 24-h net radiation total amounted to 4.10 and 4.00 MJ m^{-2}, and at the lower sidewall sites, East Lower and West Lower, to 3.33 MJ m^{-2}. Thus, the upper sidewall sites received 20%–23% more net radiative energy than the lower sidewall sites. At East Upper, the enhancement (relative to East Lower) was due to the higher receipt of K↓ (section 4b). At West Upper the enhancement (relative to West Lower) was caused primarily by the receipt of more L↓ (accounting for 16% more net radiation) and, secondarily, by a slight reduction in |L↑| (4% more net radiation). The differences discussed here arose mainly during daytime; the nighttime differences in Q^* between the lower and upper sidewall sites are small.

The largest nighttime radiation loss (AST–ASR) occurred at the Rim site (4.65 MJ m^{-2}). The longwave net radiative loss at Floor amounted to only 72% of this loss at Rim. The radiative energy loss at the west sidewall sites amounted to 82% and 83%, the one on the east sidewalls to 92% and 95% of the loss at Rim. The reduced net loss at Floor is the combination of a lower |L↑| (due to the low minimum temperatures reached at the crater bottom) and an increased L↓ (due to the contribution from radiating sidewalls). At the other sites, the reduction of the longwave net loss compared to the Rim site is mainly due to the increase in L↓, most likely caused by radiation input from the opposing sidewalls of the crater.

i. Radiation equilibria

Over flat terrain in clear-sky conditions, two equilibria in the diurnal radiation budget occur per day, one occurring approximately an hour after sunrise when K^* first exceeds $|L^*|$, and one occurring an hour or more before sunset when the diminishing K^* drops below $|L^*|$ (Fig. 4). Over sloping surfaces, the equilibria are shifted much closer in time to the local sunrise and sunset times by the sudden increase or decrease in K^* when the slope goes out of or into shadow. For example, in the morning at West Upper, K^* exceeds $|L^*|$ almost immediately after local sunrise. Similarly, in the afternoon at East Lower, K^* drops suddenly below $|L^*|$ when the shadow of the west rim falls on the site. The sudden reversal of Q^* at local sunrise and sunset reverses the surface energy balance and, after a short time, depending on the partitioning of energy into the other terms of the surface energy budget, produces warm or cold boundary layers that reverse the direction of the slope wind systems. As a result, strong horizontal gradients in the surface radiative budget move across the crater following the terminator (i.e., the edge of the shadow).

5. Discussion

Observations of short- and longwave radiation in the complex terrain of Meteor Crater were taken on radiometers oriented parallel to the underlying slopes. Horizontally oriented radiometers are inappropriate for measuring the radiation on sloping surfaces because they do not take account of the appropriate hemispherical solid angle through which radiation is received or the cosine relationship between the normal to the slope and the incoming radiation. The observational difficulties involved in making appropriate slope-parallel measurements should not be underestimated, as the slope and azimuth angles selected for the radiometer require a spatial average of the terrain around the radiometer site if the sloping surface is not strictly homogeneous.

Time integrated fluxes on radiometers over flat homogeneous terrain are usually reported as *daily* (24 h) totals and *daytime* totals from ASR to AST. Nighttime totals are determined by subtraction. This reporting is done because shortwave radiation is present only during daytime, while the longwave radiation terms are active for the entire 24-h period. For complex terrain, on the other hand, the radiation field is influenced by terrain shading (i.e., the presence of shadows from the surrounding terrain), which suggests an additional integration period from LSR to LSS. By reporting the daily, ASR–AST, and LSR–LST totals, one can determine the AST–ASR and LST–LSR totals by subtraction, allowing additional focus to be on the importance of diffuse solar radiation received before LSR and after LST.

Some of the findings can be compared with two previous studies of the radiation balance in complex terrain by Whiteman et al. (1989) and Matzinger et al. (2003).

Our observations were made in a pristine high-altitude environment. Values of $K\downarrow/K\downarrow_{ext}$ were high, comparable with the values of 0.71–0.80 for the Brush Creek Valley (1795 m MSL) reported by Whiteman et al. (1989) and larger than the values of 0.54–0.65 observed by Matzinger et al. (2003) in a valley with a floor elevation of only 250 m. The high altitude and pristine atmosphere are the causes for the minor contribution of diffuse radiation (<10%) to the total incoming shortwave flux. The contribution reported for Brush Creek was slightly higher, ranging between 11% and 14% but would have been lower for a completely clear sky (Whiteman et al. 1989).

The spatial variation of the radiation balance depends on the distribution of obstructing topography and on the terrain exposure toward the sun. Both the longwave and shortwave parts of the radiation balance are affected. The first factor affecting the shortwave part of the radiation balance is terrain shading. Shadows cast by surrounding terrain limit the receipt of direct solar radiation and thus reduce the main contribution to global radiation. In Meteor Crater, for example, the upper part of the south sidewall was shaded by the crater rim during most of the day, while the north upper sidewall was affected by terrain shading only during short time periods before astronomical sunset and after astronomical sunrise. By calculating the potential global radiation we quantified the effect of terrain shading at the different observation sites. The greatest reduction of daily shortwave radiation due to terrain shading (6%) occurred at West Lower. Terrain shading effects on the energy balance have been shown to influence the timing of inversion layer breakup and slope wind systems in idealized valleys (Colette et al. 2003).

The second factor that greatly affects the shortwave balance is the *terrain exposure* described by the slope and azimuth angles. The angle between the surface-normal and the solar beam direction determines the magnitude of the direct shortwave radiation component. Terrain exposure shifts insolation maxima toward the morning at the west and toward the evening at the east sidewalls (Whiteman et al. 1989; Matzinger et al. 2003). While the sites in Meteor Crater were generally placed on an east–west line, all but the east upper sidewall site faced several degrees north of east and consequently received less solar incoming radiation. Terrain exposure also controls the effectiveness of terrain shading. Terrain shading effects were especially strong when insolation was intense outside the shadow (i.e., when the local solar zenith angle was low), which explains why the effect of terrain shading on daily total solar incoming radiation was variable from site to site.

A third factor affecting the shortwave radiation balance in complex terrain is the enhancement of diffuse radiation at a site embedded in topography due to the *reflections from higher surrounding terrain*. This topographic effect is especially important in areas characterized by high surface albedos, such as snow-covered mountainous terrain (Chen et al. 2006; Olyphant 1986). Although the flux differences were well within the range of measurement uncertainties, our observations indicated that diffuse radiation is enhanced at the crater floor because of sidewall reflection within the basin. This topographic effect depends on the surface reflectivity and its variation within the elevated topography.

Albedo also affects K^* by determining the magnitude of shortwave reflected radiation. Higher albedo ejecta and scarce vegetation covering the Rim site (0.28 versus 0.20 elsewhere) led to lower K^* totals at Rim than at the Floor site, in spite of the terrain shading effects reducing K^* at Floor. Reflected shortwave radiation at Rim includes contributions from lower lying terrain some distance away from the site. The exposure of this terrain (toward the west) is likely to have caused the distinct diurnal cycle of albedo showing an increase through the day. Similar diurnal albedo variations were reported in the Riviera Valley (Matzinger et al. 2003) and at the west-southwest sloping site ''E'' in Brush Creek Valley (Whiteman et al. 1989).

The longwave radiation balance is influenced by direct and indirect topographic effects. The direct effects are linked to the receipt of longwave emissions from higher surrounding topography. On the other hand, topography can influence the thermal stratification of the enclosed atmosphere, for example, inversions can form in depressions, which then affects the emission from the terrain in contact with the atmosphere. The distribution of shortwave energy during daytime—influenced by topography as elaborated above—leads to a surface temperature distribution that influences the magnitude, and thus importance, of longwave radiation received from surrounding terrain.

Longwave incoming radiation $L\downarrow$ generally followed the diurnal cycle of air temperature. The variation of $L\downarrow$ among the observation sites in Meteor Crater was small, only 20 W m^{-2} at night and approximately 30 W m^{-2} during the day, illustrating a lesser effect of topography. There was a tendency for $L\downarrow$ to decrease with elevation. This tendency and the low intersite variation were also observed in Brush Creek Valley (Whiteman et al. 1989). In Meteor Crater, the lowest $L\downarrow$ occurred at the rim, with higher fluxes at the crater floor and the lower sidewall sites. Nevertheless, topographic effects on $L\downarrow$ complicated the picture. At individual sites within the crater, $L\downarrow$ depended more strongly on the radiating temperature of—and exposure to—the surrounding elevated terrain. The sites at the upper sidewalls showed higher levels of $L\downarrow$ throughout the day, receiving a significant contribution from the

thermal emission off the heated (daytime) or warmer (nighttime stable stratification) crater sidewalls in the view of the instruments. This pattern is clearly indicated by the enhanced L↓ before noon at West Upper and after noon at East Upper, during the times when insolation reached its maximum and thus the strongest surface heating occurred. Strong surface heating will lead to warmer air layers adjacent to the surface. The influence of near-surface air layers on L↓, although often neglected (Dirmhirn 1964), has previously been reported to be strong (Plüss and Ohmura 1997).

Values of L↑ are dependent on surface temperature and are thus influenced by and strongly coupled to the site-specific solar heating and the strength of sensible cooling through ventilation by the local wind field. The timing of maxima in |L↑| corresponds with the maxima in shortwave radiation receipt. During nighttime when an inversion formed in the crater, L↑ was significantly reduced at the lower elevations within the crater where temperatures were colder. In particular, the very shallow but strong surface inversion caused the 10–20 W m^{-2} lower values observed at the crater floor site. The L↑ was subject to an indirect effect of topography: if cold air can collect in a depression, the surface can cool efficiently, and a low longwave emission results. On a sloping surface, on the other hand, cooled air adjacent to the surface will drain and warmer air advected from aloft will warm the surface, resulting in a stronger longwave emission. Following sunrise, L↑ responded very quickly to increases in insolation. The matching timing of this morning increase in |L↑| with the timing of local sunrise indicated the fast response of L↑ to changes in shortwave insolation, a phenomenon previously reported by Hoch (2005).

Net radiation Q^*, the sum of all short- and longwave components, had complicated dependencies. All of the topographic effects on the individual components of the radiation balance will influence net radiation, depending on their relative strengths. At all sites in Meteor Crater, Q^* was lowest shortly after sunset when the radiating temperature differences between the atmosphere and the surface were greatest. Maximum Q^* is usually reached just before noon, as the net longwave loss is usually greatest in the afternoon while shortwave radiation peaks at solar noon. This behavior was seen at the horizontal sites at the crater floor and rim. The sloping sites showed a different picture, as they were influenced by the topographic effects of terrain exposure on the main driver of net radiation, the shortwave incoming flux. The shift of the insolation maxima toward the morning at the west and toward the evening at the east sidewalls led to a prenoon peak of Q^* at the west and postnoon peak at the east sidewalls. The distribution of Q^* within the crater topography varied remarkably, which ultimately will affect other variables in the surface energy balance such as latent and sensible heat flux. For example, on a daily basis the crater rim site received 40% less radiative energy than the basin floor site. At night, the net radiation loss was highest at the rim site; the crater floor experienced only 72% of this loss.

6. Conclusions

Components of the surface radiation budget measured at multiple sites in and around Arizona's Meteor Crater are reported for 21 October 2006, a representative clear day. Meteor Crater is a near-symmetric, bowl-shaped basin with a near–constant elevation rim. This special topography simplifies the analysis and understanding of the topographic effects that affect the different components of the radiation budget and differ from site to site.

Terrain exposure (slope and azimuth angles) led to the largest site-to-site variability, governing the receipt of direct shortwave radiation, the dominating term of the radiation budget. The measurements of diffuse radiation on the crater rim and floor indicate the enhancement of diffuse radiation within the crater basin due to the *reflection of shortwave radiation on the elevated terrain* of the crater sidewalls.

This article draws new attention to the effect of *terrain shading* in complex topography. A simple method for quantifying the effect of terrain shading on the radiation budget under clear-sky conditions is demonstrated. It was shown that sites on the lower eastern and western sidewalls of Meteor Crater are more strongly affected by terrain shading than the site on the crater floor and the steeper sites on the upper east and west sidewalls.

Counterradiation from the sidewalls enhances the longwave downward radiation at the sites within the crater basin. The difference in outgoing longwave radiation between sloping sites and the crater floor site illustrates an indirect effect of topography connected to inversion formation in enclosed topography. Cooled air will flow downhill or collect in topographic depressions, which controls the rate of surface cooling and thus the magnitude of longwave emission.

This article focused on measured radiation components in and around Meteor Crater. Future articles will focus on surface energy budget components at these measurement sites and on the modeling of the distribution of radiation and surface energy budget components over the entire crater domain. Further, dynamic feedbacks on the energy distribution such as valley wind circulations will be studied.

Acknowledgments. This research was supported by National Science Foundation Grants ATM-0444205 and

ATM-0837870. SWH was supported by Fellowship PBEZ2-113920 from the Swiss National Science Foundation and Grant 52734-EV from the Army Research Office. We thank the Barringer Crater Company and Meteor Crater Enterprises for crater access and those listed in the acknowledgments section of Whiteman et al.'s (2008) article for their help with the field program. We thank S. Oncley, S. Semmer, T. W. Horst, and W. O. J. Brown for assistance with radiation instrumentation. Javier Corripio provided the computer code to compute topographic shading. We thank the three anonymous reviewers for their comments that helped to improve the manuscript.

REFERENCES

Chen, Y., A. Hall, and K. N. Liou, 2006: Application of three-dimensional solar radiative transfer to mountains. *J. Geophys. Res.,* **111,** D21111, doi:10.1029/2006JD007163.

Colette, A., F. K. Chow, and R. L. Street, 2003: A numerical study of inversion-layer breakup and the effects of topographic shading in idealized valleys. *J. Appl. Meteor.,* **42,** 1255–1272.

Corripio, J. G., 2003: Vectorial algebra algorithms for calculating terrain parameters from DEMs and solar radiation modelling in mountainous terrain. *Int. J. Geogr. Information Sci.,* **17,** 1–23.

Dirmhirn, I., 1964: *Das Strahlungsfeld im Lebensraum.* Akademische Verlagsgesellschaft, 426 pp.

Duguay, C. R., 1993: Radiation modeling in mountainous terrain: Review and status. *Mt. Res. Dev.,* **13,** 339–357.

Hoch, S. W., 2005: Radiative flux divergence in the surface boundary layer. A study based on observations at Summit, Greenland. Ph.D. thesis, ETH, doi:10.3929/ethz-a-005163546, 164 pp.

Iziomon, M. G., H. Mayer, W. Wicke, and A. Matzarakis, 2001: Radiation balance over low-lying and mountainous areas in southwest Germany. *Theor. Appl. Climatol.,* **68,** 219–231.

Kohsiek, W., C. Liebethal, T. Foken, R. Vogt, S. P. Oncley, C. Bernhofer, and H. A. R. Debruin, 2007: The Energy Balance Experiment EBEX-2000. Part III: Behaviour and quality of the radiation measurements. *Bound.-Layer Meteor.,* **123,** 55–75.

Marty, C., 2000: Surface radiation, cloud forcing and greenhouse effect in the Alps. Ph.D. thesis, ETH, doi:10.3929/ethz-a-003897100, 141 pp.

——, R. Philipona, C. Fröhlich, and A. Ohmura, 2002: Altitude dependence of surface radiation fluxes and cloud forcing in the Alps: Results from the alpine surface radiation budget network. *Theor. Appl. Climatol.,* **72,** 137–155.

Matzinger, N., M. Andretta, E. Van Gorsel, R. Vogt, A. Ohmura, and M. W. Rotach, 2003: Surface radiation budget in an Alpine Valley. *Quart. J. Roy. Meteor. Soc.,* **129,** 877–895.

Müller, M. D., and D. Scherer, 2005: A grid- and subgrid-scale radiation parameterization of topographic effects for mesoscale weather forecast models. *Mon. Wea. Rev.,* **133,** 1431–1442.

Oliphant, A. J., R. A. Spronken-Smith, A. P. Sturman, and I. F. Owens, 2003: Spatial variability of surface radiation fluxes in mountainous terrain. *J. Appl. Meteor.,* **42,** 113–128.

Olyphant, G. A., 1986: Longwave radiation in mountainous areas and its influence on the energy balance of alpine snowfields. *Water Resour. Res.,* **22,** 62–66.

Oncley, S. P., and Coauthors, 2007: The Energy Balance Experiment EBEX-2000. Part I: Overview and energy balance. *Bound.-Layer Meteor.,* **123,** 1–28.

Philipona, R., B. Dürr, and C. Marty, 2004: Greenhouse effect and altitude gradients over the Alps - by surface longwave radiation measurements and model calculated LOR. *Theor. Appl. Climatol.,* **77,** 1–7.

Phillips, F. M., M. G. Zreda, S. S. Smith, D. Elmore, P. W. Kubik, R. I. Dorn, and D. J. Roddy, 1991: Age and geomorphic history of Meteor Crater, Arizona, from cosmogenic Cl-36 and C-14 in rock varnish. *Geochim. Cosmochim. Acta,* **55,** 2695–2698.

Plüss, C., and A. Ohmura, 1997: Longwave radiation on snow-covered mountainous surfaces. *J. Appl. Meteor.,* **36,** 818–824.

Whiteman, C. D., K. J. Allwine, L. J. Fritschen, M. M. Orgill, and J. R. Simpson, 1989: Deep valley radiation and surface energy budget microclimates. Part I: Radiation. *J. Appl. Meteor.,* **28,** 414–426.

——, and Coauthors, 2008: METCRAX 2006: Meteorological experiments in Arizona's Meteor Crater. *Bull. Amer. Meteor. Soc.,* **89,** 1665–1680.